Environmental Research Letters

LETTER • OPEN ACCESS

A chlorophyll-deficient, highly reflective soybean mutant: radiative forcing and yield gaps

View the article online for updates and enhancements.

Environmental Research Letters

A chlorophyll-deficient, highly reflective soybean mutant: radiative forcing and yield gaps

L Genesio[1], R M Bright[2] , G Alberti[1,3], A Peressotti[3], G Delle Vedove[3], G Incerti[3], P Toscano[1], M Rinaldi[4], O Muller[5] and F Miglietta[1]

1 Institute of Bioeconomy, National Research Council (CNR-IBE), Via Caproni 8 50145, Florence, Italy
2 Norwegian Institute of Bioeconomy Research Høgskoleveien 8 1433, Ås, Norway
3 Department of Agricultural, Food, Environmental and Animal Sciences, University of Udine, Via delle Scienze 206 33100, Udine, Italy
4 Cereal and industrial crops Research Centre, Council for Agricultural Research and Economics, S.S. 673, km 25, 200 71122, Foggia, Italy
5 Institute of Bio- and Geosciences, IBG-2: Plant Sciences, Forschungszentrum Jülich GmbH 52425, Jülich, Germany

E-mail: giorgio.alberti@uniud.it

Keywords: albedo change, radiation management, MinnGold, climate change mitigation

Abstract

Sunlight absorbed at the Earth's surface is re-emitted as longwave radiation. Increasing atmospheric concentrations of CO_2 and other greenhouse gases trap an increasing fraction of such heat, leading to global climate change. Here we show that when a chlorophyll (Chl)-deficient soybean mutant is grown in the field, the fraction of solar-irradiance which is reflected, rather than absorbed, is consistently higher than in commercial varieties. But, while the effect on radiative forcing during the crop cycle at the scale of the individual experimental plot was found to be large (-4.1 ± 0.6 W m^{-2}), global substitution of the current varieties with this genotype would cause a small increase in global surface albedo, resulting in a global shortwave radiative forcing of -0.003 W m^{-2}, corresponding to 4.4 Gt CO_2eq.

At present, this offsetting effect would come at the expense of reductions to yields, probably associated with different dynamic of photosynthetic response in the Chl-deficient mutant. The idea of reducing surface-driven radiative forcing by means of Chl-deficient crops therefore requires that novel high-yielding and high-albedo crops are made available soon.

1. Introduction

Croplands currently occupy 11.97% of the global land surface (FAO 2020). Agriculture must maintain or increase crop yields (greater production over a smaller land surface), while maximizing its environmental benefits. For instance, specific agronomic measures may increase carbon sequestration in soils by reduced or no-tillage cultivation methods (Lal 2004, Mayer *et al* 2018) or increase the surface albedo of croplands by means of residue management (Davin *et al* 2014) while not reducing yield levels. Increases in albedo (the ratio between reflected and incoming shortwave irradiance) may contribute to reducing the current increase in longwave radiative forcing (RF_{LW}) which is caused by the rise of atmospheric well-mixed greenhouse gases (GHGs; by 3.1 W m^{-2} in 2015 since the pre-industrial era) (Lenton and Vaughan 2009, Myhre *et al* 2017, Mayer *et al* 2018). Modelling experiments have repeatedly shown that higher cropland albedo may effectively mitigate the magnitude of future heatwaves—and global warming in general (Ridgwell *et al* 2009, Zamft and Conrado 2015)—by lowering near-surface air temperatures (Seneviratne *et al* 2018).

Enhanced plant glaucousness due to thicker waxy layers of leaves and/or an increased density of leaf trichomes has been considered as a possible strategy for bioengineering of albedo (Ridgwell *et al* 2009, Seneviratne *et al* 2018) even though such a possibility has only been investigated in model experiments based on largely untested assumptions about the actual albedo-changing potential of croplands. In addition , chlorophyll (Chl)-deficient crops may provide a straightforward option for increasing the albedo, potentially also leading to increased crop yields. In fact, Chl deficiency causes a reduction of light absorption, with leaves both reflecting and transmitting more light than the wild-types (Slattery *et al* 2017). At the same time, Chl

Figure 1. Large plots cultivated with Eiko (right) and MinnGold (left) in Udine in 2016.

deficiency may potentially increase canopy photosynthesis by enabling a better distribution of light within the leaf and the canopy space (Ort *et al* 2015) as well as increasing the photosynthetic efficiency and productivity through a reduction of light-harvesting antenna size and consequent reduction of the wasteful non-photochemical dissipation of excitation energy (Drewry *et al* 2014, Long *et al* 2015, Kirst *et al* 2018).

In this work, we used a spontaneous Chl-deficient soybean mutant, MinnGold, which was isolated at the University of Minnesota, USA (Campbell *et al* 2014). Seeds of this mutant were multiplied in a sufficient amount to enable field experimentation (figure 1). Leaf- and canopy-scale investigations showed that the steady-state photosynthesis of the mutant was almost identical to that of a commercial variety (Eiko), while shortwave reflectance was significantly enhanced (Sakowska *et al* 2018). Accordingly, MinnGold was considered a good candidate for exploring, also by means of direct experimentation, the climate change mitigation potential of changes in crop albedo, bearing in mind that future improved high-yielding Chl-deficient crops may become available soon.

Here we report on the albedo-enhancing effect of MinnGold and its impact on local surface and planetary energy budgets. We further report on its global impact on short-wave radiating forcing (RF_{SW}) and potential for CO_2 RF_{LW} offset from hypothetical deployment throughout the main global soybean regions. Results are based on collaborative, multi-annual and multi-site field trials that were made across Europe. Yields of the mutant along a wide latitudinal gradient are also discussed.

2. Materials and methods

2.1. Multi-site field trial

A multi-site field trial was made in summer 2016 at four locations in Europe along a north–south transect in a fully randomized experimental design with three commercial soybean varieties (Eiko, Ascasubi, Bahia) and MinnGold with four replicates. All the considered varieties show the same physiological maturity date and thus belong to the same Maturity Group (i.e. MG 1). Detailed information on the four locations are available in table 1. Soybean was grown in 14 m^2 plots (8 m $\times$ 1.8 m) at a density of 60 plants m^{-2}. Plants were sampled at stage R5 (beginning seed) (Fehr and Caviness 1977) and the plots were manually harvested at full maturity, which was reached at different dates depending on the site (table 2). The seeds were mechanically separated, dried and weighed. Differences among varieties and sites were tested using a two-way analysis of variance after checking for data normality and equality of the variances.

Table 1. Soil and climatological data for the multi-site field experiment in 2016.

Site	Site name	Latitude	Longitude	Altitude (m a.s.l.)	Soil texture	Mean annual air temperature (°C)	Annual rainfall (mm)
IT-BN	Klein-Altendorf	50.61	6.99	186	Sandy loam	10.1	774
IT-UD	Udine	46.04	13.22	88	Loam	12.8	1341
IT-FI	Fagna	43.98	11.35	241	Loam	14.5	864
IT-FG	Foggia	41.48	15.55	77	Sandy clay loam	15.8	506

Table 2. Total dry aboveground biomass at R5 stage (g m^{-2}) and dry seed yield at harvest (g m^{-2}) in 2016 at each experimental site. Mean ± standard error ($n = 4$). Different superscript lowercase letters indicate a significant difference among cultivars; different superscript capital letters indicate a significant difference among sites ($p < 0.05$). I-FG, Foggia, Italy; I-FI, Firenze, Italy; I-UD, Udine, Italy; D-KA, Klein-Altendorf, Bonn, Germany.

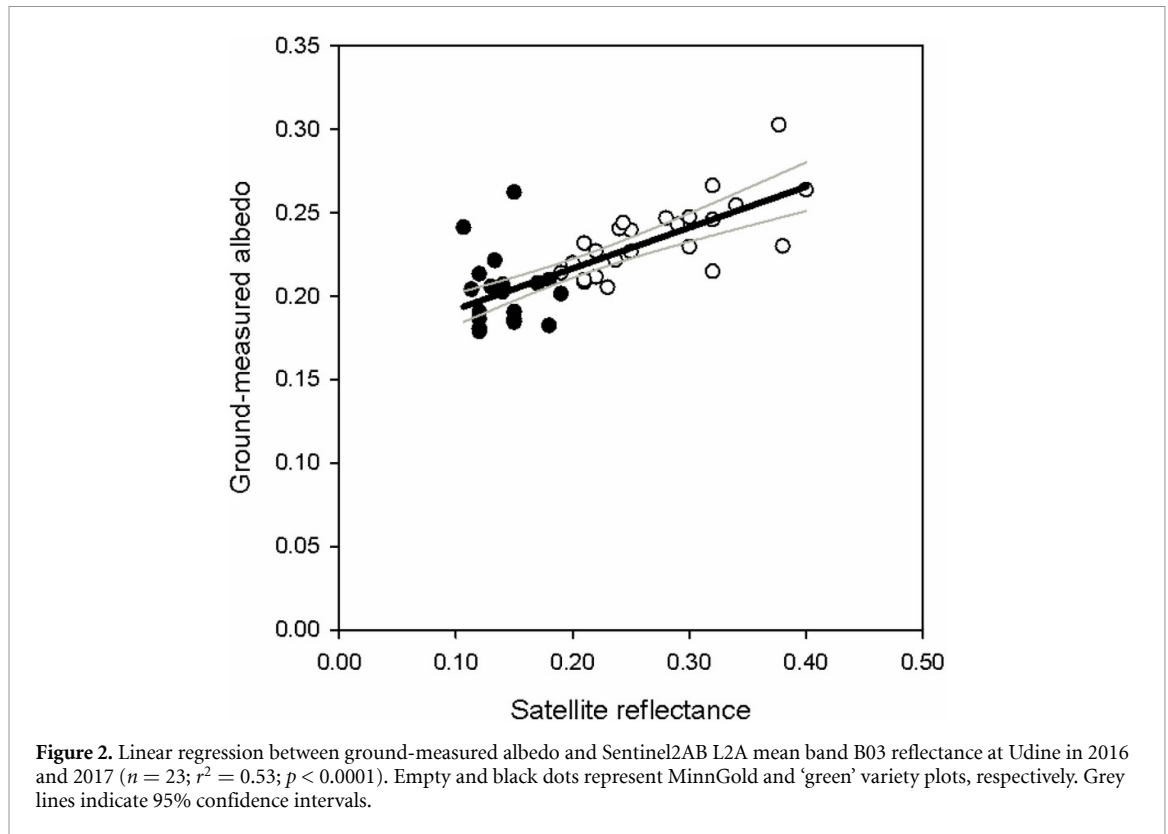|	I-FG	I-FI	I-UD	D-KA	
Latitude/longitude	41.48/15.55	43.98/11.35	46.03/13.22	50.61/6.99	
Sowing date	16 May	18 May	18 May	12 May	
Harvest date	29 Sept	6–17 Oct	23 Sept–6 Oct	11–25 Oct	
Biomass at R5 stage (g m^{-2})					**Mean for cultivar**
Ascasubi	1092 ± 179[a,A]	538 ± 56[ab,B]	1024 ± 150[a,A]	775 ± 71[a,AB]	857 ± 159[a]
Bahia	1166 ± 80[a,A]	674 ± 54[a,B]	857 ± 147[ab,AB]	714 ± 24[a,B]	853 ± 128[a]
Eiko	1032 ± 114[a,A]	577 ± 29[ab,B]	723 ± 83[ab,AB]	774 ± 89[a,AB]	776 ± 114[a]
MinnGold	882 ± 49[a,A]	453 ± 23[b,B]	622 ± 72[b,AB]	496 ± 39[b,B]	613 ± 97[b]
Mean site	1043 ± 117[A]	560 ± 56[C]	807 ± 132[B]	690 ± 81[B]	
% Biomass MinnGold vs 'green'	−20%	−24%	−28%	−34%	−26%
Seed yield at harvest (g m^{-2})					**Mean for cultivar**
Ascasubi	93 ± 9[a,A]	257 ± 34[a,B]	320 ± 6[a,B]	147 ± 9[a,A]	204 ± 49[a]
Bahia	159 ± 17[b,A]	286 ± 17[a,B]	327 ± 20[a,B]	181 ± 47[a,A]	238 ± 44[a]
Eiko	108 ± 15[ab,A]	301 ± 53[a,B]	358 ± 34[a,B]	135 ± 19[a,A]	226 ± 63[a]
MinnGold	135 ± 20[ab,A]	208 ± 16[a,AB]	268 ± 23[a,B]	45 ± 8[b,C]	164 ± 46[b]
Mean site	124 ± 19[A]	263 ± 35[B]	318 ± 26[B]	127 ± 35[A]	
% Yield MinnGold vs 'green'	12%	−26%	−20%	−71%	−26%

2.2. Albedo field and satellite measurements

Experiments aimed at investigations of albedo effects with MinnGold were made for three consecutive seasons (2016, 2017 and 2018). Two paired large plots were planted in 2016 and 2018 with MinnGold and a commercial 'green' variety at the University of Udine experimental farm (0.42 ha each) and in 2017 at the nearby De Eccher agricultural farm in Ariis (45°51′59.18″N, 13°5′22.57″ E; 3.3 ha each). The commercial variety Eiko was used in 2016 and DekaBig in 2017 and 2018 (figure 1). In 2016 and 2017, albedo was measured in those field pairs with two cross-calibrated net radiometers (CNR1, Kipp and Zonen, Delft, the Netherlands). To upscale those point measurements to entire fields in order to capture the within-plot variability, the ground-measured albedo values were correlated with simultaneous and co-located single-pixel measurements of the mean surface reflectance as measured by the Copernicus Sentinel 2A and 2B satellites. The radiometric footprint of field-deployed net radiometers installed at a height of 2 m above the canopy is comparable to the size of a satellite pixel (Marcolla and Cescatti 2018). The number of satellite pixels that were averaged to obtain the mean surface reflectance of the different field plots were >40, >500 and >30 pixels in 2016, 2017 and

2018, respectively. The satellite data (orthorectified bottom-of-atmosphere reflectances; L2A) were extracted from the 'Sentinel Hub EO browser' facility (www.sentinel-hub.com/explore/eobrowser). Only clear sky days were retained for satellite analysis (14 acquisitions in 2016, 31 in 2017 and 19 in 2018). Since most of the leaf-scale differences in reflectance between the mutant and the green varieties is in the green visible band of the spectrum (Sakowska *et al* 2018), the best correlation between ground and satellite data was found in the B03 Sentinel 2 band centered at 560 nm, bandwidth 45.5 nm (figure 2). The regression coefficients were then used to reconstruct albedo differences between MinnGold and the green varieties from all the available satellite images across the entire growing seasons in all three years and two locations.

2.3. Local radiative forcing calculations and uncertainties

Differences in daily growing season albedos between MinnGold and the commercial cultivars were then used together with irradiance data measured locally to estimate local daily mean, growing season mean and annual mean instantaneous radiative forcing for 2016, 2017 and 2018 using the radiative kernel parameterization of Bright and O'Halloran (2019):

Figure 2. Linear regression between ground-measured albedo and Sentinel2AB L2A mean band B03 reflectance at Udine in 2016 and 2017 ($n = 23$; $r^2 = 0.53$; $p < 0.0001$). Empty and black dots represent MinnGold and 'green' variety plots, respectively. Grey lines indicate 95% confidence intervals.

$$RF_d = -K_\alpha^{BO19}\Delta\alpha_d = -SW_{\downarrow,d}^{sfc}\sqrt{T_d}\Delta\alpha_d \quad (1)$$

where $SW_\downarrow^{sfc}$ is the daily solar radiation flux incident at the field site in Udine, T is the observed daily mean clearness index at the field site in Udine (or $SW_\downarrow^{sfc}/SW_\downarrow^{toa}$) and $\Delta\alpha$ is the reconstructed surface albedo difference between MinnGold and the reference. The mean daily incoming extraterrestrial solar radiation ($SW_\downarrow^{toa}$) on a horizontal surface is calculated following Duffie and Beckman (2013, Equation 1.10.3) using measured irradiances from SORCE TIM (Kopp 2019).

Errors associated with the *RF* kernel (i.e. K_α^{BO19}) and empirical $\Delta\alpha$ models are combined with the radiometer measurement uncertainty (i.e. of $SW_\downarrow^{sfc}$)

and extraterrestrial radiation uncertainty (i.e. $SW_\downarrow^{toa}$ which is used to estimate the clearness index) to arrive at single estimate of total propagated daily *RF* uncertainty for each of the three growing seasons:

$$\delta(RF_d) = |RF_d|\sqrt{\left(\frac{\delta(K_\alpha^{BO19})}{K_{\alpha,d}^{BO19}}\right)^2 + \left(\frac{\delta(\Delta\alpha)}{\Delta\alpha_d}\right)^2} \quad (2)$$

where $\delta(\Delta\alpha)$ is the error of the daily $\Delta\alpha$ regression model (equation (5)) taken as the root mean squared error given in table 4, and $\delta(K_\alpha^{BO19})$ is the combined uncertainty of the radiative kernel estimate taking into account the dependence between $SW_\downarrow^{sfc}$ and $SW_\downarrow^{toa}$:

$$\delta\left(K_\alpha^{BO19}\right) = \delta_{ME}\left(K_\alpha^{BO19}\right) +$$

$$\sqrt{\left(\frac{\partial K_\alpha^{BO19}}{\partial SW_\downarrow^{sfc}}\right)^2 \delta\left(SW_\downarrow^{sfc}\right)^2 + \left(\frac{\partial K_\alpha^{BO19}}{\partial SW_\downarrow^{toa}}\right)^2 \delta\left(SW_\downarrow^{toa}\right)^2 + \sqrt{\left(2\frac{\partial K_\alpha^{BO19}}{\partial SW_\downarrow^{sfc}}\frac{\partial K_\alpha^{BO19}}{\partial SW_\downarrow^{toa}}\sigma\left(SW_\downarrow^{sfc},SW_\downarrow^{sfc}\right)\right)^2}} \quad (3)$$

where $\delta_{ME}\left(K_\alpha^{BO19}\right)$ is the monthly model error reported in Bright and O'Halloran (2019) of the K_α^{BO19} kernel model downscaled to a daily resolution via linear interpolation (in W m^{-2}), $\delta\left(SW_\downarrow^{sfc}\right)$ is the radiometer uncertainty (10%) (Kipp and Zonen

2002, Michel *et al* 2008), $\delta\left(SW_\downarrow^{toa}\right)$ is the uncertainty of the $SW_\downarrow^{toa}$ estimate accounting for measurement uncertainty of the SORCE TIM irradiances and σ is the covariance between $SW_\downarrow^{sfc}$ and $SW_\downarrow^{toa}$.

Table 3. Soybean production area in 2000 and 2017 (ha) and relative change (Δ%) (USDA 2018).

	2000	2017	Change
Middle East	81 714	408 571	500%
Africa	913 903	38 383 916	4200%
North America	29 754 966	39 725 624	129%
South America	16 984 042	55 749 728	226%
EU-27	561 575	1 746 496	311%
Russian Federation	526 394	3 574 214	679%
China	9 545 946	8 114 056	85%
India	6 818 811	12 342 054	181%
Southeast Asia	1 221 905	830 896	68%
Oceania	35 957	11 147	31%

Table 4. Regression parameters and summary statistics for local RF_{SW} estimated as in figure 4.

Parameter	Value (standard eror)
k_0	12.24 (0.18, 25.1)
k_1	−71.26 (−183.6, 40.8)
k_2	200.9 (−143.2, 567.2)
k_3	1.30 (−9.2, 11.8)
k_4	1.99 (−2.1, 6.1)
$\boldsymbol{R^2}$	0.76
RMSE (rRMSE)	6.89×10^{-3} (35%)

2.4. Global present-day soybean production extent and intensity

Global spatial distribution of soybean production was based on the 10 km × 10 km gridded product of Monfreda *et al* (2008) providing information about the mean spatial extent (in ha) and harvest area intensity (in ha per grid cell) of soybean production activities centered around the year 2000, where harvest intensity was assumed to correspond to the area under soybean production. Soybean production area statistics at a regionally aggregated level for the year 2017 (USDA 2018) were used to re-scale year 2000 harvest area intensities in the following manner:

$$
HA_p^{2017} = \begin{cases} \frac{PA_x^{2017}}{PA_x^{2000}} HA_p^{2000} & \frac{PA_x^{2017}}{PA_x^{2000}} HA_p^{2000} 0.90 A_p \\ 0.90 A_p & \frac{PA_x^{2017}}{PA_x^{2000}} HA_p^{2000} < 0.90 A_p \end{cases} \quad (4)
$$

where HA_p^{2000} is the harvested area of the Monfreda *et al* (2008) product in pixel p, A_p is the total area of pixel p, and PA_x^{2017} and PA_x^{2000} are the reported production areas for aggregate region x (shown in table 3).

Note that because we are re-scaling the intensity and not the extent of soybean production area, growth in soybean production from 2000 to 2017 was constrained to a maximum of 90% of the pixel area. This constraint was applied to 0.3% of all pixels containing soy production.

2.5. Regional surface albedo change

It is important to emphasize that trial plots for MinnGold and the commercial varieties were jointly located at each field site and hence share the same soil background. Thus, the reconstructed differences in surface albedo ($\Delta\alpha$) between MinnGold and the commercial varieties were solely attributable to differences in leaf-level optical properties and canopy architecture. This conveniently enables transferability of $\Delta\alpha$ to other regions with different soil backgrounds. To take into account differences in growing season lengths in other regions, we constructed an empirical model based on nonlinear ordinary least squares regression of $\Delta\alpha$ and growing season lengths

observed at our field sites:

$$
\Delta\alpha(d) = \frac{d}{GLS} \frac{1 + \left(\frac{d}{GSL}\right)^{k_3}\left(1 - \left(\frac{d}{GSL}\right)^{k_4}\right)}{k_0 + k_1\left(\frac{d}{GSL}\right) + k_2\left(\frac{d}{GSL}\right)^2} \quad (5)
$$

where

GSL is growing season length (in number of days),

d is the number of days following shoot emergence and

k_n are fit parameters reported in table 4 together with associated uncertainty.

Here, regional mean sowing and harvesting dates for soybean (AMIS 2018) were used to define regional gowing season lengths (GSLs; table 5), which were subsequently used as input to the empirical model (equation (5)). Given the absence of information surrounding the timing of shoot emergence following sowing, we assume that the mean sowing date corresponded to the day of first shoot emergence ($d = 1$).

2.6. Global radiative forcing

'All-sky' albedo change radiative kernels from CAM5 (Pendergrass *et al* 2018) were used to link local $\Delta\alpha$ at the surface to local shortwave radiative flux changes at the top of the atmosphere. The CAM5 kernel was chosen over others because its spatial resolution (0.94° × 1.25°) is the highest of all existing kernels (e.g. HadGEM2, CAM3, ECHAM6) and because the atmospheric state variables used to derive it was closest to the present-day state (i.e. 2006–2007) of all existing kernels. The radiative kernels—provided at a monthly mean temporal resolution—were first downscaled by the nearest-neighbor method to the spatial resolution of the soy production grid (10 km × 10 km) and subsequently re-sampled to the daily temporal resolution via linear interpolation.

The annual mean instantaneous shortwave radiative forcing for any given grid cell (or pixel) was computed as:

$$
RF_{p,SW} = 100 \left[365^{-1} \sum_{d=1}^{365} K_{p,d,\Delta\alpha}^{CAM5} \Delta\alpha_{p,d}\right] \frac{A_{p,Soy}}{A_p} \quad (6)
$$

where $A_{p,Soy}$ is the area under soy production in pixel p (in m²), A_p is the total pixel area in pixel p (in m²),

Table 5. Soybean regional mean sowing and harvesting dates (DOY, day of year) used to estimate growing season length (*GSL*) (AMIS 2018).

	Mean sowing date (DOY)	Sowing range days ($\pm$)	Mean harvest date (DOY)	Harvest range days ($\pm$)
Middle East	135	45	288	45
Africa	334	30	59	30
North America	151	30	255	40
South America	319	60	105	60
EU-27	120	30	273	30
Russian Federation	120	30	273	40
China	135	45	273	30
India	181	30	273	30
Southeast Asia	288; 90	45; 180	90; 273	240; 45
Oceania	319	45	105	45

$K_{p,d,\Delta\alpha}^{CAM5}$ is the CAM5 albedo change shortwave radiative kernel [in W m^{-2} $(-0.01\Delta\alpha)^{-1}$] for pixel p and day d, and $\Delta\alpha_{p,d}$ is the surface albedo change for pixel p and day d.

2.7. CO_2 equivalence

Locally, comparison with a well-mixed GHG like CO_2 requires normalizing the annual mean instantaneous *RF* in each grid cell to the Earth's total surface area:

$$RF_{p,SW}^{Global} = 100 \left[365^{-1} \sum_{d=1}^{365} K_{p,d,\Delta\alpha}^{CAM5} \Delta\alpha_{p,d} \right] \frac{A_{p,Soy}}{A_{Earth}} \tag{7}$$

where A_{Earth} is the surface area of the Earth or 5.10072×10^{14} m^2. We compute the grid cell CO_2 equivalence following Betts (2000) as:

$$CO_2 eq_{p,\Delta\alpha} = RF_{p,SW}^{Global} \left(RF_{CO_2,kg} AF \right)^{-1} \tag{8}$$

where *AF* is the airborne fraction for 2017 computed following Raupach *et al* (2014) using the latest global carbon budget numbers from Le Quéré *et al* (2018) and with $RF_{CO_2,kg}$ as the radiative efficiency of CO_2 per kg computed following Myhre *et al* (2013) as:

$$RF_{CO_2,kg} = \frac{5.35 \ln\left[(C_0 + 1)/C_0\right]}{1 \times 10^{-6} M_{CO_2}/M_{air} M_{atm}} \tag{9}$$

where C_0 is the global mean CO_2 concentration at the start of 2017 (404.12 ppmv), M_{CO_2} is the molecular weight of CO_2 (44.009 kg kmol^{-1}), M_{air} is the molecular weight of air (28.97 kg kmol^{-1}) and M_{atm} is the mass of the atmosphere (5.1441×10^{18} kg), giving a radiative efficiency of 1.6925×10^{-15} W m^{-2} kg^{-1}.

2.8. Eddy covariance experiment

This experiment was run at the De Eccher agricultural farm in Ariis. MinnGold and DekaBig were sown on 27 May 2017 in three replicated irrigated plots (average size 3.3 ha) at a density of 48 plants m^{-2}. A weather station was placed in two of the selected plots (one MinnGold and one wildtype) and equipped to measure air temperature and humidity (HMP45AC, Vaisala), rainfall (7852 Davis rain gauge, Davis Instruments, USA), soil temperature at 5 cm depth using six type T thermocouples, soil water content (0–20 cm) using one time-domain reflectometer (TDR CS616, Campbell Scientific, Logan, UT, USA), incoming and reflected shortwave radiation and incoming and outgoing longwave radiation using a four-band net radiometer (CNR-1, Kipp and Zonen). All variables were measured at 2 Hz and then averaged half-hourly using a CR1000 datalogger (Campbell Scientific). Additionally, incoming photon flux density (PPFD) was measured at 2 Hz using a LI-190 quantum sensor (LiCor, Lincoln, NE, USA).

An eddy covariance tower was installed in the same two plots to assess mass, momentum and energy fluxes. The measurement height was 1.75 m. Each eddy covariance tower was equipped with a sonic anemometer (CSAT-3, Campbell Scientific) and an open path infrared gas analyzer (Li-7500A, LiCor). Both the anemometer and the Li-7500A pointed south and the northward, eastward and vertical separations between the two instruments were 18.0, 16.5 and 5 cm, respectively. Data from the sonic anemometer and the open path IRGA were recorded at a frequency of 20 Hz and stored on the LI-7550 Analyzer Interface Unit. Ecosystem fluxes of CO_2 (net ecosystem exchange, NEE; μmol CO_2 m^{-2} s^{-1}), momentum, sensible heat (W m^{-2}) and latent heat (W m^{-2}) were averaged on a half-hourly basis. The applied methodology was based on the Euroflux protocol (Aubinet *et al* 1999) with the Webb–Pearman–Leuning correction (Webb *et al* 1980). All the post-processing and frequency response corrections were made using EddyPro 6.2.1 (LiCor) and quality assessment and quality check analysis (QA/QC) were made according to Mauder and Foken (2006). Footprint analysis was performed according to Kljun *et al* (2004) and data were discarded and not considered for further analysis when at least 70% of the flux did not originate within each of the selected plots. Moreover, all original data flagged with a quality indicator > 1 (e.g. with non-turbulent conditions)

Table 6. Number of half-hour eddy data used to quantify the effect of photosynthetic photon flux density (PPFD) fluctuations on gross primary productivity by date.

	Number of half-hour eddy data between 09:00 and 13:30 UTC			
Date	MinnGold	Wildtype	Min. PPFD	Max. PPFD
25/07/2017	9	9	1422	1784
26/07/2017	–	–	–	–
27/07/2017	9	9	1416	1716
28/07/2017	10	10	1434	1768
29/07/2017	–	–	–	–
30/07/2017	–	–	–	–
31/07/2017	9	9	1353	1705
01/08/2017	9	9	1320	1688
02/08/2017	–	–	–	–
03/08/2017	7	7	1290	1682
04/08/2017	10	10	1277	1655
05/08/2017	9	9	1269	1651
06/08/2017	10	10	1301	1662
07/08/2017	–	–	–	–
08/08/2017	–	–	–	–
09/08/2017	10	10	1230	1583
10/08/2017	–	–	–	–
11/08/2017	7	7	1309	1652
Total	**99**	**99**	–	–

were dismissed. Ecosystem respiration was assessed using night-time flux data, which were selected according to a global radiation threshold of 10 W m^{-2} (nights below that threshold), cross-checked against sunrise and sunset data derived from the local time. All these fluxes were defined as ecosystem respiration (R_{eco}; μmol m^{-2} s^{-1}). An exponential equation was then fitted to the scatter of R_{eco} versus air temperature (T_{air}; °C):

$$R_{eco} = a \, e^{bT_{air}}. \tag{10}$$

Using half-hour air temperature, R_{eco} was computed during the day and gross primary productivity (GPP; μmol m^{-2} s^{-1}) was derived as:

$$GPP = -NEE + R_{eco}. \tag{11}$$

To better describe the effect of light fluctuations on GPP, we considered only the period between canopy closure (LAI $\geqslant$ 3 m^2 m^{-2}) and maximum LAI (LAI = 4.5 m^2 m^{-2}) between 25 July and 18 August 2017. Only the central part of the day (09:00–13:30 UTC) was considered to avoid any possible light limitation on photosynthesis. For the same reason, only periods in which mean half-hour PPFD was at least 1200 μmol m^{-2} s^{-1} were considered. In total, we selected 99 half-hours with GPP values available for both cultivars (table 6).

PPFD fluctuations in each of the selected half hour were quantified in terms of coefficient of variation (i.e. CV = standard deviation:mean). Then, CV
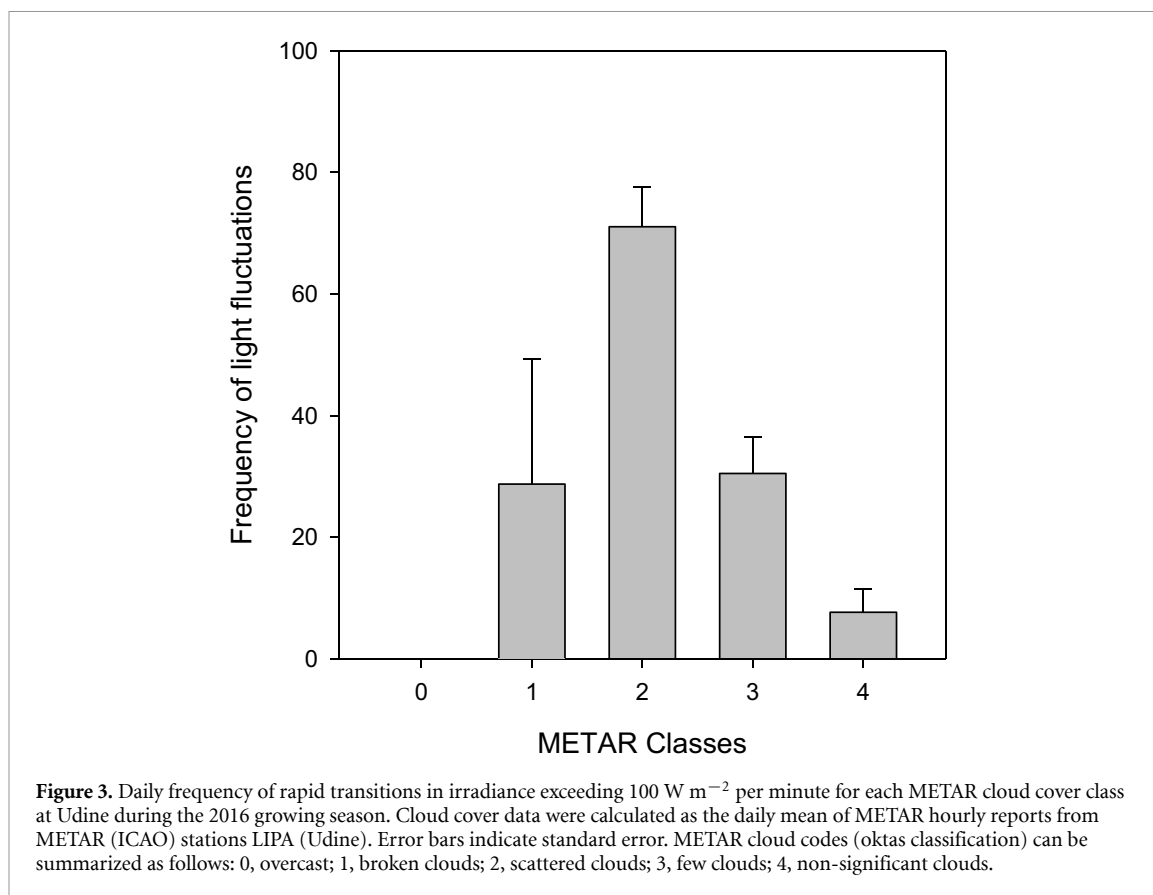
values were classified in 0.2 classes and the corresponding GPP averages were calculated. The different GPP response to PPFD fluctuations for each variety was finally calculated by linear regression. All analyses were done using STATA 10 (StataCorp, USA).

2.9. Light fluctuation estimates from meteorological data

Previous studies have shown that the Chl-deficient mutant MinnGold shows a slower relaxation of non-photochemical quenching during rapid transitions from high to low light (Sakowska *et al* 2018). Light fluctuations were not measured in detail at all the sites in the field trial, and hence the peculiar light fluctuation regimes which naturally occur under broken or scattered cloud conditions at each site could not be assessed. Light fluctuations were therefore indirectly estimated on the basis of the visual reporting of specific cloud cover types from METAR records of the ICAO (meteorological aerodrome reports of the International Civil Aviation Organization) that were made at the airport closest to each experimental site [Klein–Altendorf (Germany), code EDDK, distance from the field site 27 km; Udine (Italy), code LIPA distance from the field site 11 km; Firenze (Italy), code LIRQ, distance from the field site 21 km; Foggia (Italy), code LIBA, distance from the field site 12 km]. The visual classification of sky conditions in METAR is reported on half-hour reporting of a combination of observations ranging from completely clear to overcast skies. In our case, the METAR observations were further classified into five main classes ranging from completely overcast sky conditions (0) to broken clouds (1), scattered clouds (2), few clouds (3) and no significant clouds (4). At one of the experimental sites (Udine, Italy), the irradiance was measured at sufficiently high frequency (1 min) in both 2016 and 2017. This enabled us to calculate on a daily basis a light fluctuation index (LFI), expressed as the daily sum of rapid transitions in irradiance exceeding 100 W m^{-2}. The LFI is obviously zero when the sky is both completely overcast and completely clear, while it reaches a maximum under scattered cloud conditions or, in other terms, when light fluctuations due to the alternation of high and low light conditions are frequent (figure 3).

3. Results and discussion

Shortwave reflectance measurements based on both field and satellite data in 2016, 2017 and 2018 showed that the albedo of MinnGold was consistently higher than the albedo of the green varieties (figure 4). When the canopies were fully developed, the differences in albedo were as large as 0.055, 0.051 and 0.044, respectively, in the three consecutive years. These differences, when averaged, equated to a mean local RF_{SW} of -4.1 ± 0.6 W m^{-2} during the crop cycle and -1.0 ± 0.1 W m^{-2} when averaged over the full

Figure 3. Daily frequency of rapid transitions in irradiance exceeding 100 W m^{-2} per minute for each METAR cloud cover class at Udine during the 2016 growing season. Cloud cover data were calculated as the daily mean of METAR hourly reports from METAR (ICAO) stations LIPA (Udine). Error bars indicate standard error. METAR cloud codes (oktas classification) can be summarized as follows: 0, overcast; 1, broken clouds; 2, scattered clouds; 3, few clouds; 4, non-significant clouds.

year, with the latter corresponding to a mean CO_2eq removal of -27.4 ± 2.1 t CO_2eq ha^{-1}. Temporal patterns of RF_{SW} from sowing to harvest and associated uncertainties are shown for the three years in figure 5. From a mitigation perspective, if such a local effect was extended to all the arable lands of the Friuli-Venezia Giulia region (300 kha), where soybean cultivation extends over 55 kha (ISTAT 2020), and if permanency was ensured, this would lead to a mitigation potential equivalent to -1.5 Mt CO_2eq. Such a mitigation could be eventually added to other CO_2 removals and offsets associated with farm-based climate smart agronomic practices. It is also possible that other co-benefits may be associated with such local-scale effects such as, for instance, a reduction in water use by the crop or direct cooling of the air, in particular during heatwaves (Davin *et al* 2014). Those effects, however, have not been considered in detail in this study.

As far as global effects are concerned, the US Department of Agriculture estimates that the world soybean production area extended over 160 Mha in 2017, a 240% increase since 2000 (table 4). The mean annual RF_{SW} that could be attained over this area by substituting the current soybean varieties with the highly reflective MinnGold mutant is calculated to be equal to -0.04 W m^{-2}, with a local minimum of -1.69 W m^{-2} occurring in areas where soybean is densely cultivated and solar irradiance during the growing season is the highest (figure 6). Expressed in

terms of radiatively equivalent CO_2 emissions, these mean and minimum RF_{SW} values equate to roughly -1 and -44 t CO_2eq ha^{-1}, respectively.

Taken collectively, this amounts to -4.4 Gt CO_2eq globally which corresponds to 85% of the 2014 global CO_2 equivalent emissions from agriculture (table 7), the same order of magnitude as the estimated carbon sequestration potential in croplands through agricultural management for a single year (-6.52 Gt CO_2eq y^{-1}) (Mayer *et al* 2018). In a multi-year perspective, however, it is obvious that CO_2 emission mitigation practices may vastly outweigh that afforded by the enhanced surface albedo of soybean; however, it is worth noting that soybean is just one of a myriad of staple crops spanning Earth's surface, and the advent of other kinds of genetically engineered crops with high surface albedos may serve to boost the bio-geophysical mitigation potential of croplands in the future, as pointed out in previous modelling studies (Ridgwell *et al* 2009, Seneviratne *et al* 2018).

On the other hand, uncertainties associated with our estimates of mitigation potential suggest some caution in drawing conclusions. The uncertainty associated with the difference in albedo between the mutant and commercial varieties is relatively small, even if unpublished data suggest that differences in albedo between the mutant and the green varieties may diminish when the global radiation levels are low. As far as our extrapolations are concerned,
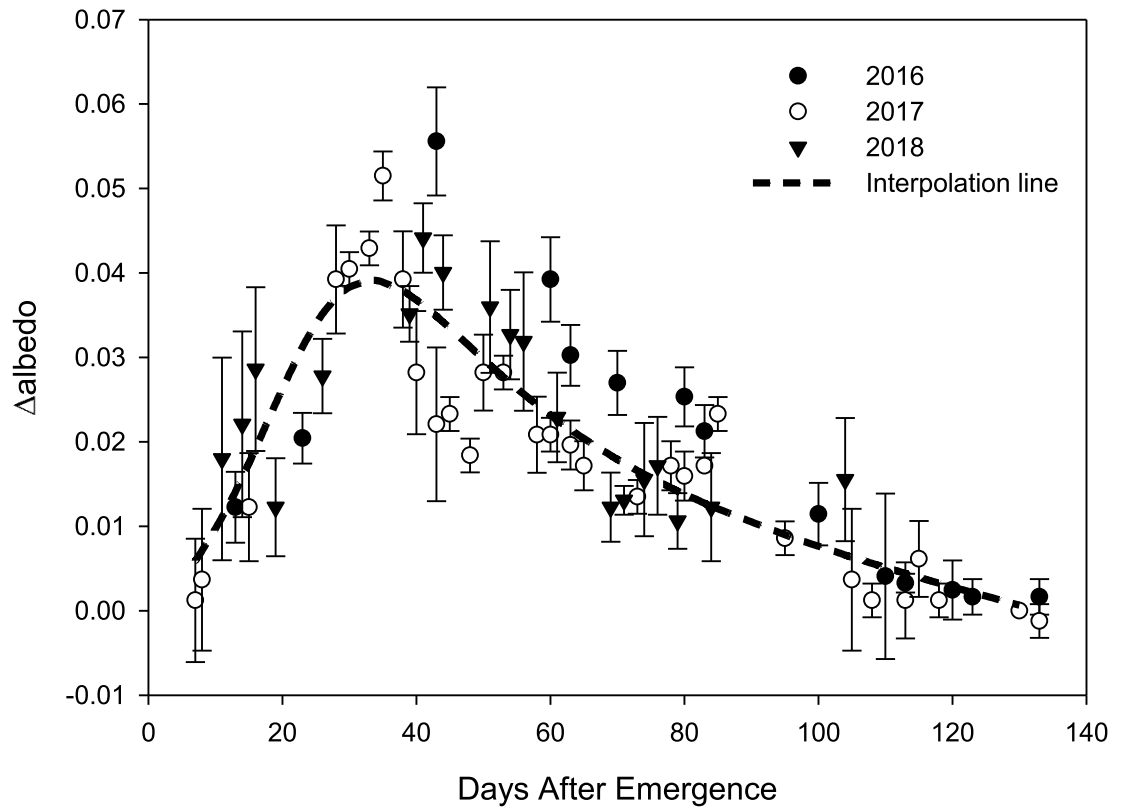
Figure 4. Differences in surface daily albedo (Δalbedo) between MinnGold and the commercial soybean varieties estimated from Sentinel 2 satellite data in Udine in 2016 ($n = 14$), 2017 ($n = 31$) and 2018 ($n = 19$). The interpolation line was obtained by means of a modified skewed Pearson probability density function. The variability of satellite values within plots is presented as standard deviation (vertical bars).
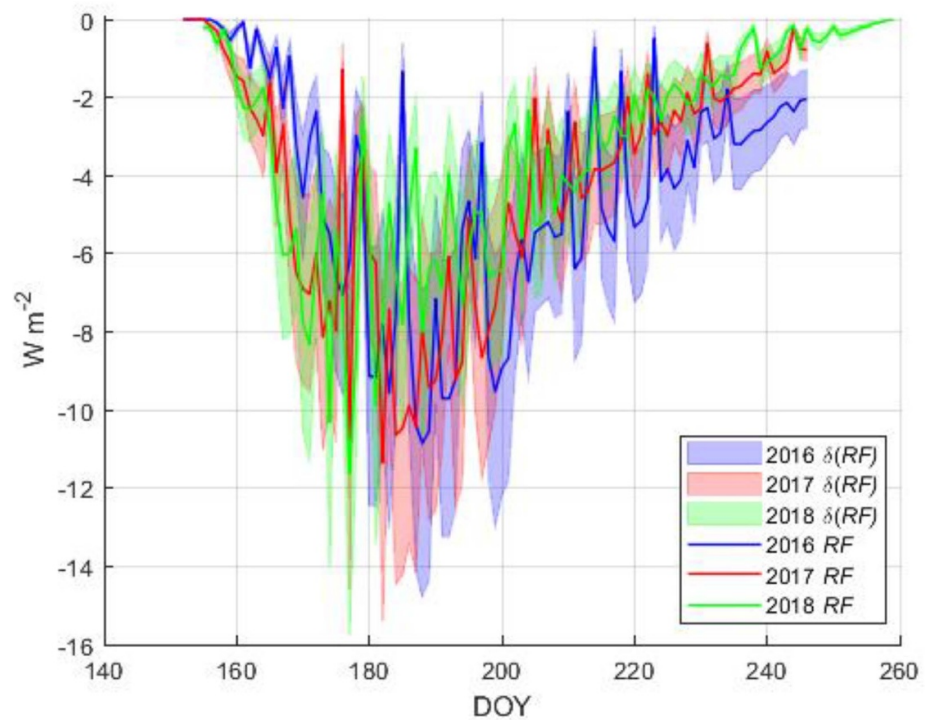

Figure 5. Local daily *RF* and its uncertainty ($\delta\,(RF)$) computed for three growing seasons at Udine.

Figure 6. Annual mean shortwave radiative forcing (RF_{SW}; in W m^{-2}) and CO_2 equivalent effect (in kt CO_2eq) from the hypothetical surface albedo change following the conversion of all the productive soybean area to MinnGold. 'Mean' refers to the mean over the soybean area only.
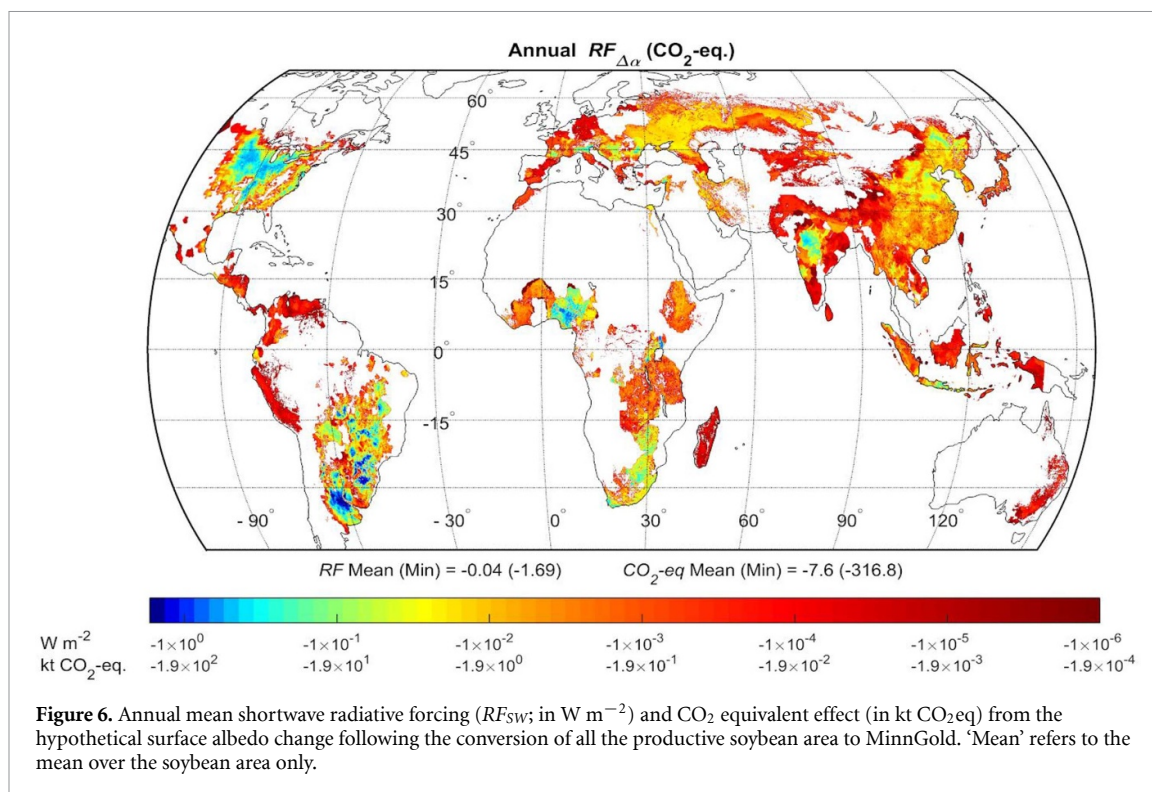
Table 7. Annual shortwave radiative forcing (RF_{SW}) due to the replacement of commercial 'green' soybean varieties with the highly reflective MinnGold mutant per macro region. Mitigation potential as Gt CO_2eq in 2017 globally and disaggregated per macro region. RF_{SW} is the mean over the soybean area only. For reference, the most recent estimate of global agricultural emissions (2014) is 5.25 Gt CO_2eq (Monfreda *et al* 2008).
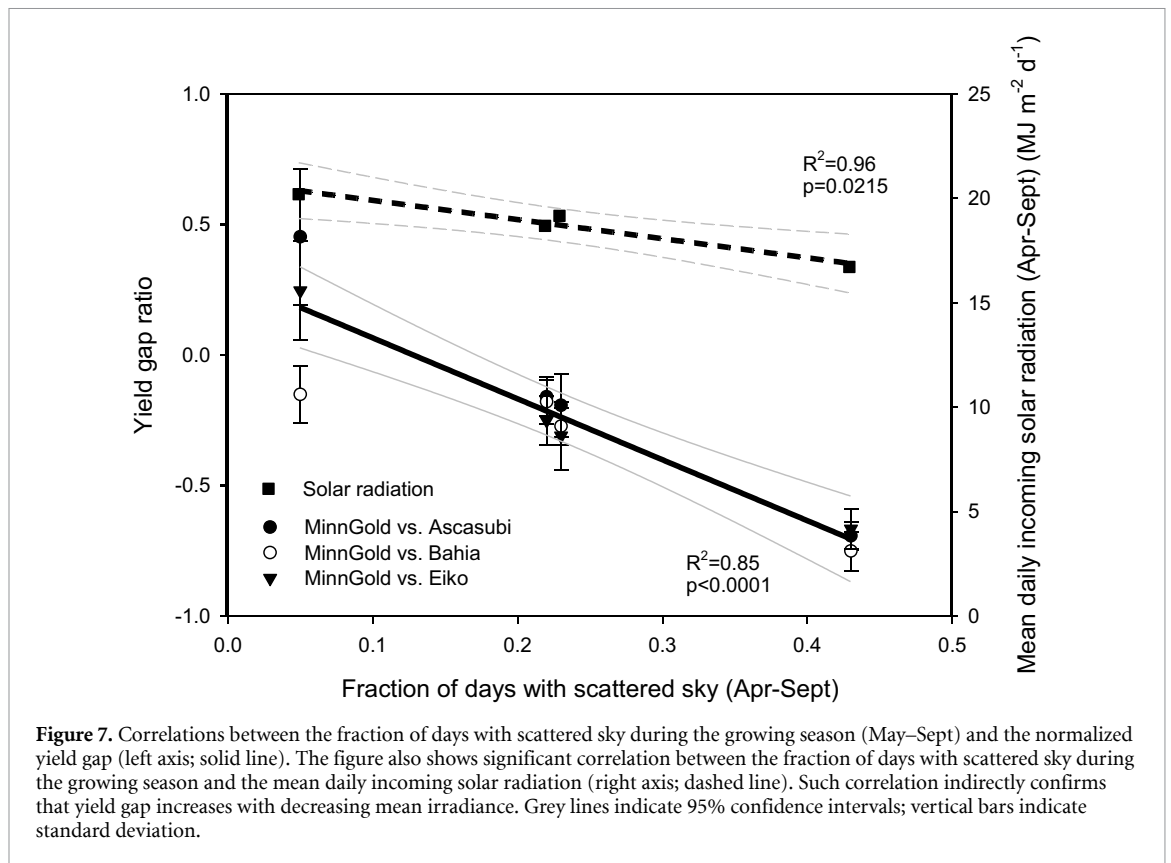
	RF_{SW}[a] (W m^{-2})	CO_2eq (Gt)
Middle East	−0.014	−0.016
Africa	−0.053	−0.724
North America	−0.110	−1.08
South America	−0.146	−1.98
EU-28	−0.016	−0.067
India	−0.024	−0.146
China	−0.014	−0.212
Russian Federation	−0.013	−0.152
Southeast Asia (includes Indonesia)	−0.009	−0.062
Oceania	−3.14E-04	−0.0005
Global	−0.040	−4.44

[a]Mean of total 2017 regional soybean production area.

a larger uncertainty comes from the methodology used to extrapolate changes in surface albedo to other regions with differing soybean crop cycles (from emergence to senescence), which may depend on many factors including air temperature, soil type, nutritional status and water availability. Moreover, temperature is a key driver of crop duration (i.e. the higher the mean temperature, the shorter the crop cycle) and this introduces another potential uncertainty considering that global temperatures are rapidly rising. Interannual fluctuations around the mean cloud cover or global incoming radiation during the crop cycle may also introduce some uncertainty, but this is likely to be of relatively minor importance.

The experimental data from our multi-site field trial showed that those theoretical radiative forcing benefits would, however, imply a cost in terms of reductions in grain yield. Indeed, the mean yield of MinnGold averaged over the four study sites in 2016 was 26% less than that of the three commercial varieties used in the comparison (table 2). This occurred in spite of the comparable photosynthetic rates that were measured at leaf and canopy scale under steady-state conditions (Sakowska *et al* 2018). It is worth noting here that the observed differences in biomass production and yield were uneven along the latitudinal gradient: MinnGold produced +12% and −71% of grain yield in the southernmost and northernmost locations, respectively (table 2). Larger yield in the southernmost locations were, however, mainly due to the fact that control varieties showed higher pod shattering, something that is well known to occur under hot and dry conditions (Gulluoglu *et al* 2006). The yield gaps between MinnGold and the green varieties were strongly correlated with irradiance (figure 7): the higher the radiation, the lower the yield gap. In northeast Italy, a region, which is considered one of the most favorable soybean production areas of Europe, the relative difference in yield between MinnGold and the three other varieties was 20%, on average (table 2). The yield and biomass production gaps observed in the multisite field trial of 2016 were confirmed for this specific site also in 2017 (figure 8).

Differential growth and production may be also related to substantial differences in dynamic photosynthesis, i.e. the ensemble of adaptive mechanisms of the photosynthetic machinery that occurs following a

Figure 7. Correlations between the fraction of days with scattered sky during the growing season (May–Sept) and the normalized yield gap (left axis; solid line). The figure also shows significant correlation between the fraction of days with scattered sky during the growing season and the mean daily incoming solar radiation (right axis; dashed line). Such correlation indirectly confirms that yield gap increases with decreasing mean irradiance. Grey lines indicate 95% confidence intervals; vertical bars indicate standard deviation.

rapid change in irradiance (Kaiser *et al* 2018). Fluctuating light conditions associated with 'cloud flecks' are supposed to reduce the growth of MinnGold in response to lower relaxation rates of photoprotection (non-photochemical quenching) following rapid transitions between illuminated and shaded conditions (Sakowska *et al* 2018). Mass and energy fluxes measured by eddy covariance in Italy in 2017 strongly confirm such a hypothesis. Light fluctuations, expressed as the coefficient of variation of the incoming PPFD during the time of the measurements, did not affect the GPP of the green cultivar, but dramatically reduced the GPP of MinnGold (figure 9). By inference, the gap in biomass and yield between the mutant and the commercial varieties can be assumed to increase with increasing light fluctuations that naturally occurr under broken or scattered cloud conditions (figure 7). Taking into account that the maturity class was the same across the considered soybean varieties at all experimental sites, this effect may tentatively explain why the yield gap was higher in the northern regions of Europe.

4. Conclusions

Our study demonstrates that Chl-deficient mutants such as MinnGold would be a readily deployable and scalable land radiation management technology that could eventually contribute to mitigation of GHG emissions at the local scale: albedo changes would be large and persistent throughout the duration of the growing season and would provide a simple and readily applicable strategy for farmers to boost their mitigation efforts. Such mitigation effects would increase with increasing incoming radiation—or in places where clear sky conditions prevail over cloudy sky conditions. Moreover, the albedo enhancement may provide other important climate benefits at the local scale, as proposed elsewhere for heat wave mitigation (Davin *et al* 2014).

When seen in a global perspective, our data lead to three main conclusions:

(i) Large increases in canopy surface albedo, which have been considered in recent modelling studies, are likely to be overestimated: the mean seasonal albedo increase ($\Delta\alpha$) with one of the most reflective Chl-deficient crops, such as MinnGold, does not exceed 0.02 (α from 0.24 to 0.26). Whatever the case, increased shortwave reflectance is unavoidably associated with reduced light absorption by photosynthetic pigments. The idea that the surface albedo can be further enhanced without substantial negative effects on yields remains a largely untested hypothesis.

(ii) The global substitution of current soybean varieties with MinnGold would translate into a relatively small global mean RF_{SW} (-0.003 W m^{-2}). While this value is negligible compared with RF_{LW} from anthropogenic
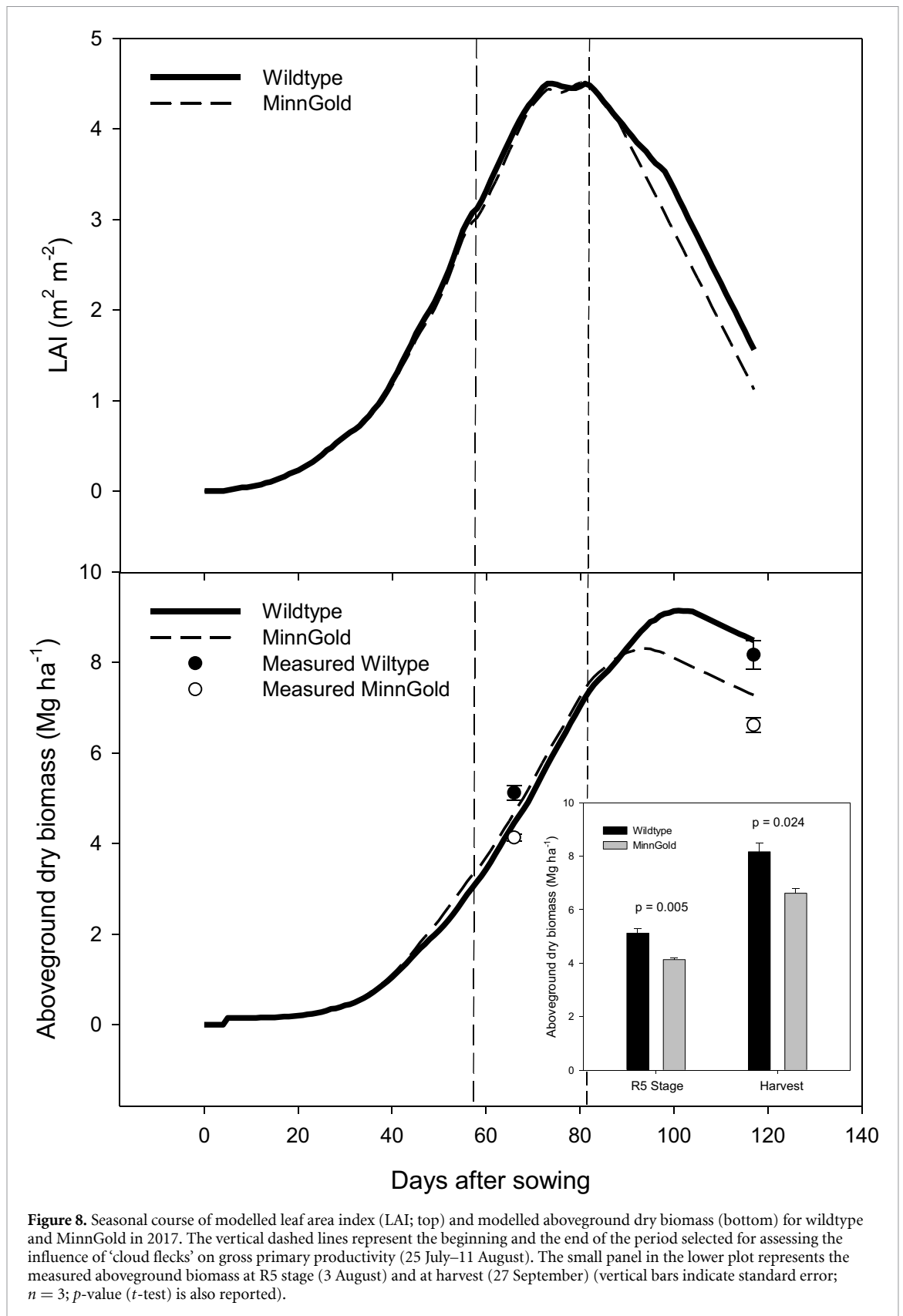
Figure 8. Seasonal course of modelled leaf area index (LAI; top) and modelled aboveground dry biomass (bottom) for wildtype and MinnGold in 2017. The vertical dashed lines represent the beginning and the end of the period selected for assessing the influence of 'cloud flecks' on gross primary productivity (25 July–11 August). The small panel in the lower plot represents the measured aboveground biomass at R5 stage (3 August) and at harvest (27 September) (vertical bars indicate standard error; $n = 3$; p-value (t-test) is also reported).

CO_2 or from all well-mixed GHGs, it provides a contribution which is likely to be potentially extended when Chl-deficient crops of other species become available and are deployed at large scale.

(iii) The trade-off between mitigation effect and reduced yields prevents immediate application of MinnGold: effective and sustainable mitigation would require in fact high-yielding Chl-deficient varieties as the critical 'food-for-all'
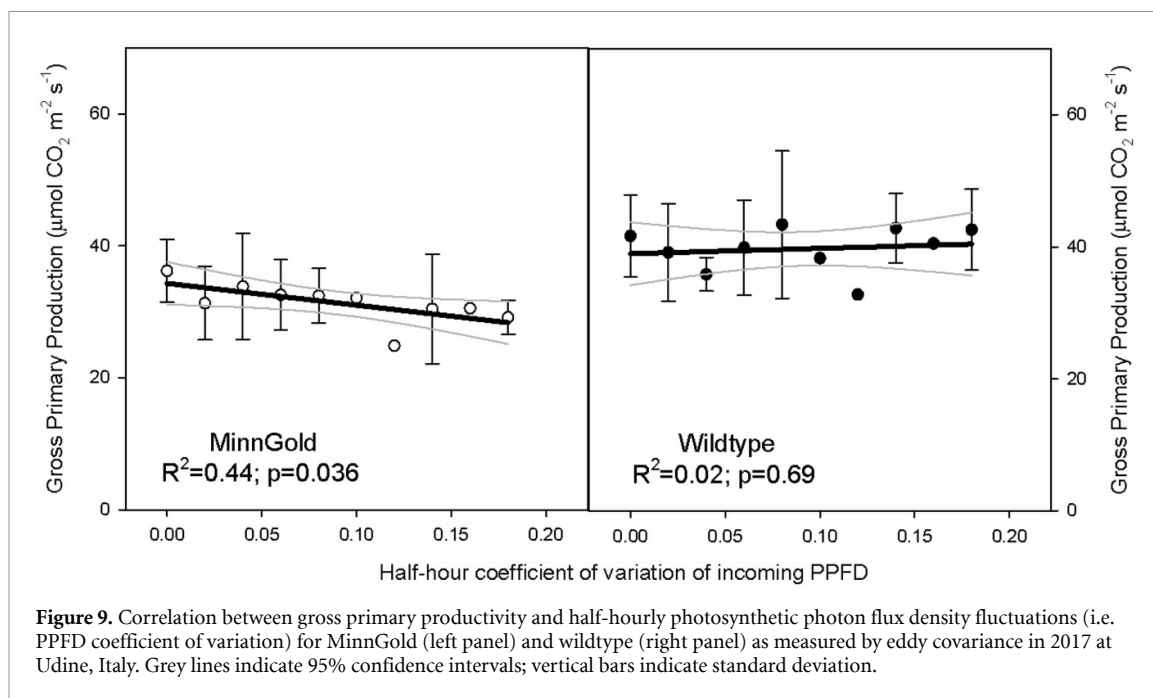
Figure 9. Correlation between gross primary productivity and half-hourly photosynthetic photon flux density fluctuations (i.e. PPFD coefficient of variation) for MinnGold (left panel) and wildtype (right panel) as measured by eddy covariance in 2017 at Udine, Italy. Grey lines indicate 95% confidence intervals; vertical bars indicate standard deviation.

goal must be achieved while fighting against ongoing changes in the climate. However, gene transfer or genome editing technologies, together with improved knowledge and understanding of basic physiological mechanisms in plants, are already promising the creation of new high-yielding Chl-deficient crops (Kirst *et al* 2017). The concept of a truncated light-harvesting antenna complex may already be applied to several crop species, including corn and soybean (Kirst *et al* 2018). Longer crop duration or delayed senescence in annuals should also be an important trait to combine with higher crop reflectivity. But the creation of high-yielding Chl-deficient perennial species should be a priority target, as those species would ensure longer crop duration and, with this, a higher mitigation potential.

Acknowledgments

Funding

Author contributions

Competing interests

The authors declare no competing interests.

Data availability statement

The data that support the findings of this study are available upon request from the authors.

ORCID iD

R M Bright ⓘ https://orcid.org/0000-0001-8553-5570

References

AMIS 2018 Agricultural market information system 2018 Soybeans: planting and harvesting calendar (available at: www.amis-outlook.org/amisabout/calendars/soybeancal/en/ (Accessed: 9 November 2018)

Aubinet M *et al* 1999 Estimates of the annual net carbon and water exchange of forests: the EUROFLUX Methodology *Adv. Ecol. Res.* **30** 113–75

Betts R A 2000 Offset of the potential carbon sink from boreal forestation by decreases in surface albedo *Nature* **408** 187–90

Bright R M, Bogren W, Bernier P and Astrup R 2016 Carbon-equivalent metrics for albedo changes in land

management contexts: relevance of the time dimension *Ecol. Appl.* **26** 1868–80

Campbell B W, Mani D, Curtin S J, Slattery R A, Michno J M, Ort D and Stupar R M 2014 Identical substitutions in magnesium chelatase paralogs result in chlorophyll-deficient soybean mutants *G3–Genes Genom. Genet.* **5** 123–31

Davin E L, Seneviratne S I, Ciais P, Olioso A and Wang T 2014 Preferential cooling of hot extremes from cropland albedo management *Proc. Natl Acad. Sci. USA* **111** 9757–61

Drewry D T, Kumar P and Long S P 2014 Simultaneous improvement in productivity, water use, and albedo through crop structural modification *Glob. Change Biol.* **20** 1955–67

Duffie J A and Beckman W A 2013 *Solar Engineering of Thermal Processes* 4th edn (New York: Wiley) pp 928

FAO 2020 Land use indicators www.fao.org/faostat/en/#data/EL (Accessed: 11 March 2020)

Fehr W R and Caviness C E 1977 Stages of soybean development *Iowa Coop. Ext. Serv. Spec. Rep.* **80** 1–12

Gulluoglu L, Arioglu H and Arslan M 2006 Effects of some plant growth regulators and nutrient complexes on pod shattering and yield losses of soybean under hot and dry conditions *Asian J. Plant Sci.* **5** 368–72

Kaiser E, Morales A and Harbinson J 2018 Fluctuating light takes crop photosynthesis on a rollercoaster ride *Plant Physiol.* **176** 977–89

Kipp and Zonen 2002 Instruction manual CNR1 net radiometer manual version 0706 (available at: www.kippzonen.com/pages/706/3)

Kirst H, Gabilly S T, Niyogi K K, Lemaux P G and Melis A 2017 Photosynthetic antenna engineering to improve crop yields *Planta* **245** 1009–20

Kirst H, Shen Y, Vamvaka E, Betterle N, Xu D Warek U *et al* 2018 Downregulation of the CpSRP43 gene expression confers a truncated light-harvesting antenna (TLA) and enhances biomass and leaf-to-stem ratio in *Nicotiana tabacum* canopies *Planta* **248** 139–54

Kljun N, Calanca P, Rotach M W and Schmid H P 2004 A simple parameterisation for flux footprint predictions *Boundary-Layer Meteorol.* **112** 503–23

Kopp G 2019. SORCE level 3 total solar irradiance daily means version 018 (Greenbelt, MD: NASA Goddard Earth Science Data and Information Services Center (GES DISC)) (https://doi.org/10.5067/D959YZ53XQ4C) (Accessed: 31 March 2020)

Lal R 2004 Soil carbon sequestration impacts on global climate change and food security *Science* **304** 1623–7

Le Quéré C, Andrew R M Friedlingstein P *et al* 2018 Global carbon budget 2018 *Earth Syst. Sci. Data.* **10** 2141–94

Lenton T M and Vaughan N E 2009 The radiative forcing potential of different climate geoengineering options *Atmos. Chem. Phys. Discuss.* **9** 2559–608

Long S P, Marshall-Colon A and Zhu X G 2015 Meeting the global food demand of the future by engineering crop photosynthesis and yield potential *Cell* **161** 56–66

Marcolla B and Cescatti A 2018 Geometry of the hemispherical radiometric footprint over plant canopies *Theor. Appl. Climatol.* **134** 981–90

Mauder M and Foken T 2006 Impact of post-field data processing on eddy covariance flux estimates and energy balance closure *Meteorol. Z.* **15** 597–609

Mayer A, Hausfather Z, Jones A D and Silver W L 2018 The potential of agricultural land management to contribute to lower global surface temperatures *Sci. Adv.* **4** eaaq0932

Michel D, Philipona R, Ruckstuhl C, Vogt R and Vuilleumier L 2008 Performance and uncertainty of CNR1 net radiometers during a one-year field comparison *J. Atmos. Oceanic Technol.* **25** 442–51

Monfreda C, Ramankutty N and Foley J A 2008 Farming the planet: 2. Geographic distribution of crop areas, yields, physiological types, and net primary production in the year 2000 *Global Biogeochem. Cycles* **22**

Myhre G *et al* 2013 Anthropogenic and natural radiative forcing supplementary material *Climate Change 2013: The Physical Science Basis. Contribution of Working Group I to the Fifth Assessment Report of the Intergovernmental Panel on Climate Change* ed T F Stocker *et al* (Geneva: IPCC) (available at: www.ipcc.ch)

Myhre G, Myhre C L, Forster P M and Shine K P 2017 Halfway to doubling of CO2 radiative forcing *Nat. Geosci.* **10** 710–11

Ort D R, Merchant S S, Alric J, Barkan A, Blankenship R E Bock R *et al* 2015 Redesigning photosynthesis to sustainably meet global food and bioenergy demand *Proc. Nat. Acad. Sci. USA* **112** 8529–36

Pendergrass A G, Conley A and Vitt F M 2018 Surface and top-of-atmosphere radiative feedback kernels for CESM-CAM5 *Earth Syst. Sci. Data.* **10** 317–24

Raupach M R, Gloor M Sarmiento J L *et al* 2014 The declining uptake rate of atmospheric CO_2 by land and ocean sinks *Biogeosciences* **11** 3453–75

Ridgwell A, Singarayer J S, Hetherington A M and Valdes P J 2009 Tackling regional climate change by leaf albedo bio-geoengineering *Curr. Biol.* **19** 146–50

Sakowska K *et al* 2018 Leaf and canopy photosynthesis of a chlorophyll deficient soybean mutant *Plant Cell Environ.* **41** 1427–37

Seneviratne S I, Phipps S J, Pitman A J, Hirsch A L, Davin E L, Donat M G and Kravitz B 2018 Land radiative management as contributor to regional-scale climate adaptation and mitigation *Nat. Geosci.* **11** 88–96

Slattery R, Vanloocke A, Bernacchi C, Zhu X and Ort D 2017 Photosynthesis, light use efficiency, and yield of reduced-chlorophyll soybean mutants in field conditions *Front. Plant Sci.* **8** 549

USDA 2018 Foreign Agricultural Service of the United States Department of Agriculture World Agricultural

Webb E K, Pearman G I and Leuning R 1980 Correction of flux measurements for density effects due to heat and water vapour transfer *Q. J. R. Meteorol. Soc.* **106** 85–100

Zamft B M and Conrado R J 2015 Engineering plants to reflect light: strategies for engineering water-efficient plants to adapt to a changing climate *Plant Biotechnol. J.* **13** 867–74